

# Real-Space Inversion and Super-Resolution of Ultrafast X-ray Scattering using Natural Scattering Kernels

Adi Natan<sup>1,\*</sup>

<sup>1</sup>Stanford PULSE Institute, SLAC National Accelerator Laboratory 2575 Sand Hill Road, Menlo Park, CA 94025  
(Dated: July 16, 2021)

Directly resolving in real-space multiple atomic motions using ultrafast x-ray scattering is generally limited by the finite detector range. As a result, signal interpretation mostly relies on modeling and simulations of specific excitation pathways. Here, we demonstrate an approach to resolve ultrafast diffuse x-ray scattering signals in real space and recover multiple atomic motions de-novo. We introduce a scattering basis representation that is composed of the measurement parameters and constraints, and the subsequent inversion analysis. We then leverage signal priors, such as smoothness and sparsity to deconvolve and super-resolve the spatially transformed signals using convex optimization. We validate the approach on simulated data with detection limits similar to X-ray free-electron laser experiments and discuss the resolution limits and noise dependence on the accuracy of the recovery.

Ultrafast x-ray scattering using advanced light sources is an emerging tool to probe the motion of photo-excited molecular systems at the angstrom and femtosecond scales. In recent years this method was successfully used to trace coherent motions and dynamics in molecules in the gas phase [1–7], as well as structural changes in molecules in solution after the electronic excitation [8–15]. Inversion of the scattering signal to obtain the real-space pair distribution function for these studies was limited by the available range of the scattering vector for the photon energies used. As a result, the methods that were developed to interpret the scattering signals were mostly model-based and relied on calculating and attaining trajectory statistics for the specific system under study, where retrieval of the transient structure was usually limited to a single reaction pathway. As a result, complex atomic motions that take place simultaneously and involve multiple pathways were often not resolved or discussed. The inversion of the total measured signal entails an additional degree of complexity, as it may be composed of different pairs species, where each pair contribution has to be disentangled from the overall signal to account for its respective form factors.

Here we introduce a simple model-free deconvolution approach to overcome the limitations that are imposed by a typical inversion procedure. We show how real-space recovery of multiple and complex motions can be obtained by leveraging the information that naturally arises from the experimental parameters, the measurement process, and the way it is analyzed, including for cases where several motions and types of atom pairs contribute.

X-ray Scattering of time-evolving charge densities under typical experimental conditions can be described by the static approximation [16] where the electronic scattering operator can be replaced with the elastic scattering expression. For simplicity, we assume an isotropic charge density  $\rho(R)$ , with the diffraction pattern is expressed as:

$$\frac{d\sigma}{d\Omega} = 2(2\pi)^2 \sigma_T S_0(q, t) \quad (1)$$

$$S_0(q, t) = \sum_{a,b} f_a^*(q) f_b(q) \int dR \rho(R, t) j_0(qR) \quad (2)$$

where  $\sigma_T$  is the Thompson scattering term,  $f(q)$  are the atomic form factors, and  $j_0(qR) = \sin(qR)/qR$  is zeroth order spherical Bessel function. For the case of a single atom pair, we can use the orthogonality relations of Bessel functions and invert the scattering curve  $S_0$  with the spherical Bessel transform:

$$y_0(R, t) = \int_0^\infty dq q^2 \frac{S_0(q, t) j_0(qR)}{f_1(q) f_2(q)} \quad (3)$$

Where  $y_0$  is the isotropic pair distance function. The integrand is often scaled with an exponential function  $e^{-kq^2}$  [10, 17] to serve as an effective experimental integration bound. However, the simple formalism in Eq (1 - 3) does not capture the various aspects of the measurement process of typical ultrafast scattering experiments, such as the experimental configuration, detector discretization, and signal truncation. As a result, applying Eq. 3 will contain severe resolution limitations and inversion artifacts, especially around the few angstrom length scale of molecular bonds. To address this, we shall borrow ideas from the theory of inverse problems and obtain an adaptive signal representation formalism that will be used to create a dictionary of parameterized real-space waveforms, or kernels, that naturally arise from the measurement and analysis procedure.

For simplicity we shall be assuming that the charge density  $\rho(R)$  is due to a single type of atom pair and is well defined on a finite portion of the 1-D real line  $[0, R_{max}]$ . We can approximate  $\rho(R)$  as a superposition of delta functions as follows:

\* natan@stanford.edu

$$\rho(R) \simeq \sum_m w_m \delta(R - R_m) \quad (4)$$

Where  $w_m$  is the weight of the  $R_m$  position. We define the natural scattering kernel (NSK) as the function that describes the distortion that a  $\delta(R - R_m)$  charge density undergoes in terms of the sample composition, measurement process, and analysis:

$$NSK(R_m) = \mathcal{T}_{q \rightarrow R} \{ \mathcal{M}_{q \rightarrow q} \{ \mathcal{T}_{R \rightarrow q} \{ \delta(R - R_m) \} \} \} \quad (5)$$

Where  $\mathcal{T}_{\alpha \rightarrow \beta}$  is the transformation from domain  $\alpha$  to domain  $\beta$  that includes signal discretization, and  $\mathcal{M}$  represent the measurement distortion in  $q$ -space. For the isotropic case, the first transformation is implemented using Eq. 2:

$$\mathcal{T}_{R \rightarrow q} \{ \delta(R - R_m) \} = 2f_a(q_i) f_b(q_i) j_0(q_i R_m) := s(q_i) \quad (6)$$

Here we assume detector discretization of the  $q$  coordinate, and we resample the signal at  $q_i = j_{0i} q_{max} / j_{0N}$ ,  $i=1 \dots N-1$ , where  $j_{0i}$  is the  $i^{th}$  root of  $j_0$ , and  $q_{max}$  is the upper bound in  $q$ . The distortion due to the measurement can be generally described via:

$$\mathcal{M}_{q \rightarrow q} \{ s(q_i) \} = s(q_i) * v(q_i) \cdot h(q_i) + b(q_i) := s'(q_i) \quad (7)$$

Where  $v(q) \simeq c_1 q - c_2 q^3 + c_3 q^5$  models the  $q$ -varying blur at  $q_i$  with coefficients  $c_i$  that are determined by the sample thickness and distance from the detector.  $h(q)$  is a window function that represents the detector's finite  $q$ -range as well as  $q$ -dependent signal absorption, and  $b(q)$  is a possible additive background. The transformation back to the  $R$  coordinate uses the same discretization scheme, which was applied recently for the discrete Hankel transform [18, 19], and is adapted here for the case of a discrete spherical Bessel Transform of the form:

$$\mathcal{T}_{q \rightarrow R} \{ s'(q_i) \} = \frac{q_{max}^2}{j_{0N}} \sum_{i=1}^{N-1} \mathbf{G}_{m,i} \frac{s'(q_i) q_i}{f_e(q_i)} = NSK(R_m) \quad (8)$$

where  $f_e(q_i) = f_a(q_i) f_b(q_i)$ , and the transformation matrix:

$$[\mathbf{G}]_{m,i} = 2 \frac{j_0 \left( \frac{j_{0m} j_{0i}}{j_{0N}} \right)}{j_{0N} j_1^2(j_{0i})} \quad (9)$$

The discretization and resampling that are used in Eqs. 6 – 9 were chosen to enable consistent operation rules for multiplication, modulation, and convolution between the  $R$  and  $q$  domains, when analyzing measured signals and defining the NSK representation.

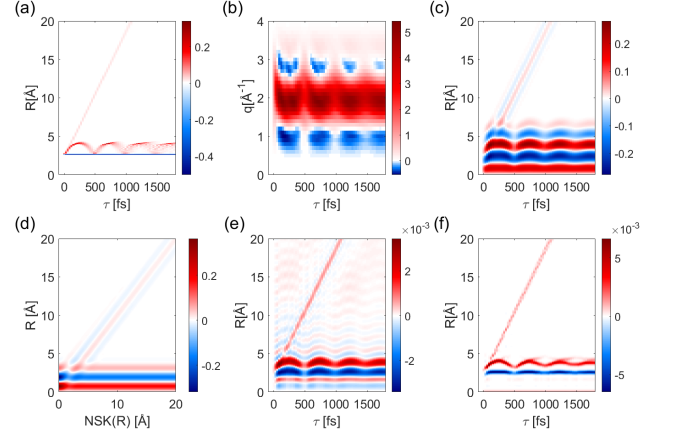


FIG. 1. (a) 1-D TDSE simulation of the time-dependent charge density difference for Iodine excited from its ground state by an 520nm , 30fs, excitation fraction of  $\sim 8\%$ , resulting in vibration and dissociation. (b) The simulated difference scattering signal assuming 20dB SNR, detector  $q$ -range truncation  $0.5 < q < 4 \text{ \AA}^{-1}$ , discretization, and resampling of  $dq = 0.1 \text{ \AA}^{-1}$  (Eq. 6-7). (c) Applying a spherical Bessel transform to the truncated scattering signal yields the pair-distribution difference signal. The limited  $q$ -range hinders the ability to accurately recover the positions and motions of the calculated charge density. (d) The NSK dictionary following the measurement constraints is used to deconvolve the pair-distribution difference using (e)  $\ell_2$  and (f)  $\ell_1$  regularizations.

We can now sample  $m=1 \dots M$  points along  $[0, R_{max}]$  to create a set of  $NSKs$  that form a dictionary  $\mathcal{D}$ , an  $M \times (N-1)$  matrix that can be used to decompose the signal under the measurement constraints. Assuming we measure a signal  $S_0(q)$ , we can resample it at the given  $q_i$  prescribed above and substitute it in Eq 8 to obtain  $y(R)$  with some noise error  $\epsilon$ . We model the measurement as:

$$\mathbf{y} = \mathcal{D} \mathbf{w} \quad (10)$$

Where we seek to estimate the weights vector  $\mathbf{w}$  to recover the measured pair density function  $y(R)$ . Naively, one would attempt to solve this model using least-squares minimization:  $\min_w \|\mathbf{y} - \mathcal{D} \mathbf{w}\|^2$ , however, this approach is highly sensitive to noise, and is generally unstable numerically when the problem is ill-posed. A standard approach for solving ill-posed inverse problems is to use a regularization framework to promote solution with properties that are based on the information of the data:

$$\min_w \|\mathbf{y} - \mathcal{D} \mathbf{w}\|^2 + \lambda \mathcal{R}(\mathbf{w}) \quad (11)$$

Where  $\lambda$  is the regularization parameter that controls the magnitude of the regularization, and the regularizer  $\mathcal{R}$  is chosen according to some prior information of the measurement to facilitates solutions with preferable features. A widely used regularization approach that addresses the numerical instabilities and produces low variance solutions is the Tikhonov or  $\ell_2$  regularization [20],

where  $\mathcal{R} = \sum_i |w_i|^2$ . Using this regularizer provides the closed form linear solution:

$$\mathbf{w} = (\mathcal{D}^T \mathcal{D} + \lambda \mathbf{1})^{-1} \mathcal{D}^T \mathbf{y} \quad (12)$$

that can be solved using singular value decomposition, where the value of  $\lambda$  can be obtained using the L-curve method [21] or by generalized cross validation [22]. The  $\ell_2$  regularization promotes solutions that are numerically stable, smooth in  $\mathbf{w}$ , and increase the ability to predict the nature of the solution. However, this usually results with most of  $\mathbf{w}$  components having non-zero values, which may reduce the ability to explicate such solutions.

For the case where we assume that the solution for  $\mathbf{w}$  is sparse, such that the number of sampling points in  $R$  that can explain the measurement  $\mathbf{y}$  is much smaller than the dimension of  $R$ , we can use the  $\ell_1$  regularized least-squares model, where  $\mathcal{R} = \sum_i |w_i|$ . This approach, is mostly known as Basis Pursuit De-Noising (BPDN) [23], or the Least Absolute Shrinkage and Selection Operator (LASSO) [24]. Its application transformed several areas of research, particularly for use cases in statistics, computer science and machine learning [25–27], signal and image processing, and compressed sensing [28–33].

The  $\ell_1$  norm has a discontinuity for  $w_i = 0$ , thus it doesn't have a closed-form solution like the  $\ell_2$  case. However, it can be solved using convex optimization, and in recent years several algorithmic approaches have evolved to address this and determine the optimal parameters [34–36]. Unlike other applications such as compressed sensing, the sparsity assumption is not sufficient for finding robust solutions in the case we present, and a further constraint of the minimum separation distance between adjacent dictionary kernels needs to be made [37, 38]. This is to avoid solution ambiguity for kernels that are closer than  $\delta R < \nu/q_{max}$ , where  $\nu = \mathcal{O}(1)$  is the separation factor that depends on signal's properties [37–39]. Otherwise, kernels that are too close in  $R$  will effectively map onto the same band-limited measurement  $s(q)$ , where their difference mostly lies beyond the detection limit  $q_{max}$ . For the case of scattering discussed here, the real-space resolution is given by  $2\pi/q_{max}$ , however, we'll show that we can resolve below this limit given signal sparsity for various SNR levels and obtain  $1.3 < \nu < 1.6$ .

To demonstrate the way NSK can be used to deconvolve real-space information from ultrafast X-ray scattering, we start with a simple case of synthetic data under typical experimental conditions. We solved a 1-D time-dependent Schrodinger equation (TDSE) for a diatomic Iodine that is excited by a 30 fs, 520 nm pulse,  $7 \times 10^{10} \text{W/cm}^2$  optical pulse, resulting in a total excitation fraction of  $\sim 8\%$ . At  $\tau=0$ , the ground  $X0_g^+$  state population at  $\sim 2.7\text{\AA}$  is excited to the bound  $B0_u^+$  state, resulting in vibration motion, and to the unbound  $C(B'')1_u$  state resulting in dissociation. We used the calculation to simulate the difference scattering signal  $\Delta S_0(q)$  for each delay. We use typical XFEL scattering geometry that uses an array detector [40] with 2M pixels, detector radius  $r=82.5\text{mm}$ , sample distance of 60mm, detector

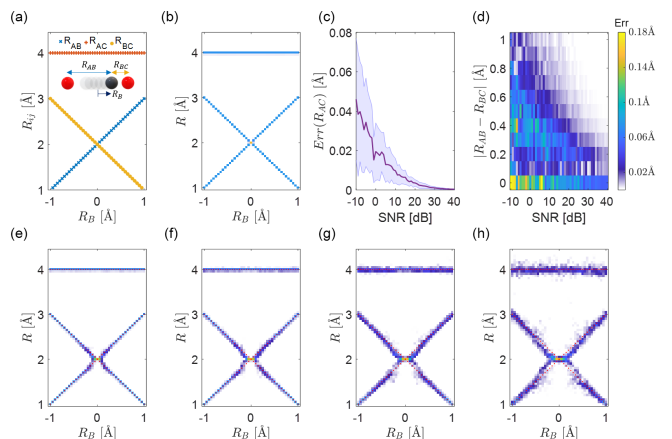


FIG. 2. Recovery accuracy under noise (a) A synthetic triatomic of atoms A,B,C is used to test the recovery accuracy around pair distances coalescence. Atoms A and C are held at  $\pm 2\text{\AA}$  while atom B is translated in the range  $[-1, 1]$ . At  $R_B = 0$  the pair distances  $R_{AB}$ ,  $R_{BC}$  coalesce. The scattering signal for each position is simulated and truncated for  $0.5 < q < 4\text{\AA}^{-1}$ . (b) We deconvolve using NSK approach with  $\ell_1$  regularization, and  $dR = 0.05\text{\AA}$  sampling. For the noiseless case, we obtain effectively an exact recovery for sampling used. (c) The average recovery error (solid), and standard deviation (shaded) as function of the SNR for  $R_{AC}$ . The recovery accuracy is  $< 0.1\text{\AA}$  across the SNR range. (d) The average recovery error as function of SNR and pair distances separation  $|R_{AB} - R_{BC}|$ . We observe that the error is proportional to the noise and the minimal distances separation, with a transition toward the coalescence point around  $\delta R \simeq 0.3 \pm 0.1\text{\AA}$ . The complete recoveries for SNR values of (e) 30, (f) 20, (g) 10, (h) 0 dB are shown with the exact distances (dotted red).

truncation for the  $q$ -range  $0.5 < q < 4\text{\AA}^{-1}$ , signal to noise ratio (SNR) of 20 dB, modeled as a  $q$ -dependent additive white Gaussian noise where each  $q_i$  bin has sampling statistics proportional to the number of detector pixels contributing to it. We used a Slepian window function [41] in the truncation range and signal resampling of  $dq = 0.1\text{\AA}^{-1}$  as described in the NSK formation process.

The result of these steps is presented in Fig 1ab. We perform the discrete spherical Bessel transform (Eq. 8) to the truncated signal and observe the limitation of the real-space inversion to recover and resolve the distances and motions of the TDSE calculation (Fig 1c). We create a dictionary  $\mathcal{D}$  with NSKs along the range  $0.1 < R < 30\text{\AA}$  with grid spacing of  $dR = 0.05\text{\AA}$  (Fig 1d). We note that in all positions of NSK( $R_m$ ) the dictionary contains an inversion artifact at  $R < 4\text{\AA}$  which is attributed to the main lobe of the transformed window function  $h(q)$ . As a result, interpretation of the inverted signal in Fig 1c is severely limited in that range, which coincidentally is of greater importance for molecular dynamics as it covers the length scale of most bonds. We used  $\mathcal{D}$  to deconvolve the weights vector of the NSK using the  $\ell_2$  regularization analytic solution in Eq. 12 (Fig 1e). We observe that

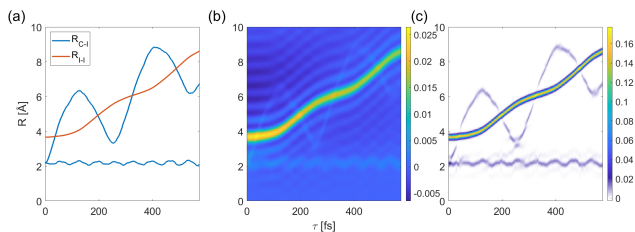


FIG. 3. (a) Trajectory calculation of the direct dissociation dynamics of  $\text{CH}_2\text{I}_2$  for I-I and C-I pair distances (taken from [42]). We simulated the scattering signal with SNR 20 dB for  $0.5 < q < 8 \text{ \AA}^{-1}$ . (b) The pair density distribution obtained using the effective form factor approximation (see text). (c) Deconvolving using the NSK approach demonstrates retrieval of the different pair density distances, where the I-I pair density signal is  $\sim \times 10$  stronger than the for the C-I pairs.

while the  $\ell_2$  approach is successful in removing many of the artifacts of the  $q$ -range truncation, and resolve the positions and motions, it has a weak ringing artifact throughout the  $R$  range used, due to the band-pass nature of the deconvolution analysis, that may reduce the ability to resolve weaker signal contributions.

We applied convex optimization for the  $\ell_1$  regularization case (Eq. 11) using CVX, a package for specifying and solving convex programs [43]. This approach not only accurately captures the real-space positions and motions but also manages to recover and super-resolve details in the dynamics such as wavepacket dispersion, while almost eliminating noise from unrelated distances. Because most of the sampling points used in  $R$  at any given time have no charge density or no motion signal, the approach illustrates the justification of the sparsity assumption for diffuse scattering signals where relatively a small number of positions in  $R$  play a role.

Since experimental measurements always contain noise, we make the distinction between noise originating from an additive source that can be modeled by an appropriate distribution to experimental artifacts that are supposed to be measured and used in the NSK formation described in Eq 7. The recovery error is expected to be significant when the separation distance  $\delta R \lesssim \nu/q_{max}$ . To test this limit we identify two possible contributions: in case of a coalescence of two (or more) pair distances, and when a pair-distance is approaching zero. Because the latter case is not physical, we focus on the recovery accuracy as a function of SNR for the case of pair distances coalescence. We use a synthetic triatomic, as described in Fig 2a, where we fixed the positions of atoms A and C at  $\pm 2 \text{ \AA}$ , while changing the position of atom B from  $-1 < R_B < 1 \text{ \AA}$ . When atom B is at  $R_B = 0 \text{ \AA}$ , the pair-distance  $R_{AB}$  will coalesce with  $R_{BC}$  at  $2 \text{ \AA}$ .

We simulate the scattering signal for each configuration of distances with the same  $q$ -range truncation and resampling of the previous system example. We apply the NSK approach first for the noiseless case and obtain an effective exact recovery for the sampling used with

negligible error at the coalescence point to adjacent  $dR$  bins (Fig 2b). We then test the recovery for a range of SNRs (-10 to 40 dB), with 20 realizations to each noise level to obtain recovery statistics. We find that the recovery accuracy for the  $\ell_1$  approach is proportional to the noise level in agreement with previous studies [37].

We observe that for the fixed  $R_{AC}$  distance the recovery error is  $< 0.1 \text{ \AA}$  across the SNRs, demonstrating the accuracy of the approach for the case of separated pair distances (Fig 2c). For the two pair distances around the coalescence point we observe that depending on the noise level there is a minimum separation distance of  $\delta R \approx 0.3 \pm 0.1 \text{ \AA}$  below which the solutions drift toward the coalescence point, with a recovery error  $< 0.2 \text{ \AA}$ . An additional limiting factor for this analysis is the sparsity assumption. We tested the recovery accuracy as a function of the number of pair distances involved and obtain the same behavior with respect to the minimal separation condition observed between pair distances. The recovery is limited by coalescence that becomes important below  $\delta R \sim 1.45/q_{max}$ . This limitation may be addressed by applying an additional real-space blur on the deconvolution results, with a blur kernel of the same magnitude to reduce the coalescence artifact effect. An alternative solution may be found in a hybrid regularization approach such as the elastic net [44] that combines both  $\ell_1$  and  $\ell_2$  norms, which is beyond the scope of this study.

Extending the approach to systems with more than a single atom pair type introduce contributions from different atom pair species with different form factors, both are not separable in the measurement process, as we only measure the total signal  $S_0(q)$ . In order to apply the NSK approach to such cases, we approximate the contributions of different atomic form factors to the form:  $f_e(q) = \sum_{a,b} f_a(q) f_b(q)$ , where  $f_e$  is defined to be the effective form factor of the overall signal  $S_0(q)$ . Because the functional form of an atom pair  $f_a(q) f_b(q)$  is a featureless monotonic function in the truncated  $q$ -range, its real-space inversion will mainly contribute to the amplitude of the main lobe at  $0 < R < \pi/q_{max}$ . As a result, the inaccuracy using the effective form factor approximation will be limited to an amplitude artifact in that range, which can be neglected as it takes place at pair distances below typical bond lengths. In addition, this form factor component contribution is stationary and doesn't enter signal difference measurements. The outcome will be a pair density distribution where atom-pairs will have an amplitude proportional to their charge densities product, and so their detection will mostly be limited by the fidelity of the measurement.

In Fig 3 we show how the NSK approach performs using trajectory calculations of the dissociation dynamics of polyatomic molecule  $\text{CH}_2\text{I}_2$  that were recently studied using ultrafast electron diffraction [42]. We used the trajectory information to simulate the X-ray scattering signal, we used a  $q$ -range similar to what was reported in the study ( $0.5 < q < 8 \text{ \AA}^{-1}$ ), and assumed an SNR of 20 dB. We employed the effective form factor approximation to

convert the scattering information to real space using Eq. 8. We then implemented the NSK approach with kernels that used the same effective form factor that was used in the real-space conversion to retrieve both  $I-I$  and  $C-I$  pair distances in agreement to the trajectory information. We note that where pair distances coalesce we obtain a similar recovery resolution as described previously, limited by the signal fidelity vs SNR for the smaller  $C-I$  pairs charge densities.

In summary, we introduce a model-free approach to recover real-space information from ultrafast diffuse X-ray scattering signals. Leveraging the measurement limitations with a consistent analysis scheme we form a dictionary of scattering kernels and use it to deconvolve the real space distorted signals. We validate this approach using ground truth TDSE and trajectory calculations to generate synthetic scattering signal with measurements constraints similar to XFEL experiments. We show that we can super-resolve simultaneous motions de-

novo and discuss the resolution limit as function of fidelity. We introduce an effective form factor approximation to demonstrate the approach for a polyatomic system with more than one type of atomic pairs. Future extensions to this approach can be done for analysis and super-resolution of anisotropic signals where real-space time-resolved analysis is needed [6], as well as using different regularization schemes and off-the-grid type approaches [45]. This approach may help bridging the successful pair-distribution function analysis that require much higher  $q$  ranges ( $q > 30 \text{ \AA}^{-1}$ ) with time-resolved high-energy 15–25 keV diffuse scattering ( $q \sim 12 \text{ \AA}^{-1}$ ) experiments that are becoming operational in XFELs.

We thank Y. Liu for the trajectory information in [42]. This work was supported by the U.S. Department of Energy, Office of Science, Basic Energy Sciences, Chemical Sciences, Geosciences, and Biosciences Division.

- 
- [1] M. P. Minitti, J. M. Budarz, A. Kirrander, J. S. Robinson, D. Ratner, T. J. Lane, D. Zhu, J. M. Glownia, M. Kozina, H. T. Lemke, M. Sikorski, Y. Feng, S. Nelson, K. Saita, B. Stankus, T. Northey, J. B. Hastings, and P. M. Weber, Imaging molecular motion: Femtosecond x-ray scattering of an electrocyclic chemical reaction, *Phys. Rev. Lett.* **114**, 255501 (2015).
- [2] J. M. Glownia, A. Natan, J. P. Cryan, R. Hartsock, M. Kozina, M. P. Minitti, S. Nelson, J. Robinson, T. Sato, T. van Driel, G. Welch, C. Weninger, D. Zhu, and P. H. Bucksbaum, Self-referenced coherent diffraction x-ray movie of ångstrom- and femtosecond-scale atomic motion, *Phys. Rev. Lett.* **117**, 153003 (2016).
- [3] B. Stankus, H. Yong, N. Zotev, J. M. Ruddock, D. Bellshaw, T. J. Lane, M. Liang, S. Boutet, S. Carbajo, J. S. Robinson, *et al.*, Ultrafast x-ray scattering reveals vibrational coherence following rydberg excitation, *Nature chemistry* **11**, 716 (2019).
- [4] J. M. Ruddock, N. Zotev, B. Stankus, H. Yong, D. Bellshaw, S. Boutet, T. J. Lane, M. Liang, S. Carbajo, W. Du, *et al.*, Simplicity beneath complexity: counting molecular electrons reveals transients and kinetics of photodissociation reactions, *Angewandte Chemie* **131**, 6437 (2019).
- [5] P. H. Bucksbaum, M. R. Ware, A. Natan, J. P. Cryan, and J. M. Glownia, Characterizing multiphoton excitation using time-resolved x-ray scattering, *Physical Review X* **10**, 011065 (2020).
- [6] A. Natan, A. Schori, G. Owolabi, J. P. Cryan, J. M. Glownia, and P. H. Bucksbaum, Resolving multiphoton processes with high-order anisotropy ultrafast x-ray scattering, *Faraday Discussions* **228**, 123 (2021).
- [7] T. Kierspel, A. Morgan, J. Wiese, T. Mullins, A. Aquila, A. Barty, R. Bean, R. Boll, S. Boutet, P. Bucksbaum, *et al.*, X-ray diffractive imaging of controlled gas-phase molecules: Toward imaging of dynamics in the molecular frame, *The Journal of Chemical Physics* **152**, 084307 (2020).
- [8] H. Ihee, Visualizing solution-phase reaction dynamics with time-resolved x-ray liquidography, *Accounts of chemical research* **42**, 356 (2009).
- [9] H. Ihee, M. Wulff, J. Kim, and S.-i. Adachi, Ultrafast x-ray scattering: structural dynamics from diatomic to protein molecules, *International Reviews in Physical Chemistry* **29**, 453 (2010).
- [10] K. H. Kim, J. G. Kim, S. Nozawa, T. Sato, K. Y. Oang, T. W. Kim, H. Ki, J. Jo, S. Park, C. Song, *et al.*, Direct observation of bond formation in solution with femtosecond x-ray scattering, *Nature* **518**, 385 (2015).
- [11] E. Biasin, T. B. van Driel, K. S. Kjær, A. O. Dohn, M. Christensen, T. Harlang, P. Vester, P. Chabera, Y. Liu, J. Uhlig, M. Pápai, Z. Németh, R. Hartsock, W. Liang, J. Zhang, R. Alonso-Mori, M. Chollet, J. M. Glownia, S. Nelson, D. Sokaras, T. A. Assefa, A. Britz, A. Galler, W. Gawelda, C. Bressler, K. J. Gaffney, H. T. Lemke, K. B. Møller, M. M. Nielsen, V. Sundström, G. Vankó, K. Wärnmark, S. E. Canton, and K. Haldrup, Femtosecond x-ray scattering study of ultrafast photoinduced structural dynamics in solvated  $[\text{Co}(\text{terpy})_2]^{2+}$ , *Phys. Rev. Lett.* **117**, 013002 (2016).
- [12] T. B. Van Driel, K. S. Kjær, R. W. Hartsock, A. O. Dohn, T. Harlang, M. Chollet, M. Christensen, W. Gawelda, N. E. Henriksen, J. G. Kim, *et al.*, Atomistic characterization of the active-site solvation dynamics of a model photocatalyst, *Nature communications* **7**, 1 (2016).
- [13] M. Chollet, R. Alonso-Mori, M. Cammarata, D. Damiani, J. Defever, J. T. Delor, Y. Feng, J. M. Glownia, J. B. Langton, S. Nelson, and *et al.*, The x-ray pump-probe instrument at the linac coherent light source, *Journal of Synchrotron Radiation* **22**, 503–507 (2015).
- [14] K. Haldrup, G. Levi, E. Biasin, P. Vester, M. G. Laursen, F. Beyer, K. S. Kjær, T. Brandt van Driel, T. Harlang, A. O. Dohn, R. J. Hartsock, S. Nelson, J. M. Glownia, H. T. Lemke, M. Christensen, K. J. Gaffney, N. E. Henriksen, K. B. Møller, and M. M. Nielsen, Ultrafast x-ray scattering measurements of coherent structural dynamics on the ground-state potential energy surface of a diplatinum molecule, *Phys. Rev. Lett.* **122**, 063001 (2019).

- [15] M. R. Panman, E. Biasin, O. Berntsson, M. Hermann, S. Niebling, A. J. Hughes, J. Kübel, K. Atkovska, E. Gustavsson, A. Nimmrich, *et al.*, Observing the structural evolution in the photodissociation of diodomethane with femtosecond solution x-ray scattering, *Physical Review Letters* **125**, 226001 (2020).
- [16] U. Lorenz, K. B. Möller, and N. E. Henriksen, Theory of time-resolved inelastic x-ray diffraction, *Phys. Rev. A* **81**, 023422 (2010).
- [17] J. C. Williamson and A. H. Zewail, Ultrafast electron diffraction. 4. molecular structures and coherent dynamics, *The Journal of Physical Chemistry* **98**, 2766 (1994).
- [18] N. Baddour and U. Chouinard, Theory and operational rules for the discrete hankel transform, *J. Opt. Soc. Am. A* **32**, 611 (2015).
- [19] N. Baddour and U. Chouinard, Matlab code for the discrete hankel transform, *Journal of Open Research Software* **5** (2017).
- [20] G. H. Golub, P. C. Hansen, and D. P. O’Leary, Tikhonov regularization and total least squares, *SIAM journal on matrix analysis and applications* **21**, 185 (1999).
- [21] P. C. Hansen and D. P. O’Leary, The use of the l-curve in the regularization of discrete ill-posed problems, *SIAM journal on scientific computing* **14**, 1487 (1993).
- [22] P. C. Hansen, *Rank-deficient and discrete ill-posed problems: numerical aspects of linear inversion* (SIAM, 1998).
- [23] S. Chen and D. Donoho, Basis pursuit, in *Proceedings of 1994 28th Asilomar Conference on Signals, Systems and Computers*, Vol. 1 (IEEE, 1994) pp. 41–44.
- [24] R. Tibshirani, Regression shrinkage and selection via the lasso, *Journal of the Royal Statistical Society: Series B (Methodological)* **58**, 267 (1996).
- [25] H. Lee, A. Battle, R. Raina, and A. Y. Ng, Efficient sparse coding algorithms, in *Advances in neural information processing systems* (Citeseer, 2007) pp. 801–808.
- [26] J. Mairal, F. Bach, J. Ponce, and G. Sapiro, Online dictionary learning for sparse coding, in *Proceedings of the 26th annual international conference on machine learning* (2009) pp. 689–696.
- [27] K. Gregor and Y. LeCun, Learning fast approximations of sparse coding, in *Proceedings of the 27th international conference on international conference on machine learning* (2010) pp. 399–406.
- [28] D. L. Donoho, Compressed sensing, *IEEE Transactions on information theory* **52**, 1289 (2006).
- [29] E. J. Candès, J. Romberg, and T. Tao, Robust uncertainty principles: Exact signal reconstruction from highly incomplete frequency information, *IEEE Transactions on information theory* **52**, 489 (2006).
- [30] M. Lustig, D. Donoho, and J. M. Pauly, Sparse mri: The application of compressed sensing for rapid mr imaging, *Magnetic Resonance in Medicine: An Official Journal of the International Society for Magnetic Resonance in Medicine* **58**, 1182 (2007).
- [31] M. F. Duarte, M. A. Davenport, D. Takhar, J. N. Laska, T. Sun, K. F. Kelly, and R. G. Baraniuk, Single-pixel imaging via compressive sampling, *IEEE signal processing magazine* **25**, 83 (2008).
- [32] O. Katz, Y. Bromberg, and Y. Silberberg, Compressive ghost imaging, *Applied Physics Letters* **95**, 131110 (2009).
- [33] T. Driver, S. Li, E. G. Champenois, J. Duris, D. Ratner, T. J. Lane, P. Rosenberger, A. Al-Haddad, V. Averbukh, T. Barnard, *et al.*, Attosecond transient absorption spooktscopy: a ghost imaging approach to ultrafast absorption spectroscopy, *Physical Chemistry Chemical Physics* **22**, 2704 (2020).
- [34] S. Boyd, N. Parikh, and E. Chu, *Distributed optimization and statistical learning via the alternating direction method of multipliers* (Now Publishers Inc, 2011).
- [35] N. Parikh and S. Boyd, Proximal algorithms, *Foundations and Trends in optimization* **1**, 127 (2014).
- [36] E. Candès and J. Romberg, l1-magic: Recovery of sparse signals via convex programming, URL: [www.acm.caltech.edu/l1magic/downloads/l1magic.pdf](http://www.acm.caltech.edu/l1magic/downloads/l1magic.pdf) **4**, 14 (2005).
- [37] E. J. Candès and C. Fernandez-Granda, Super-resolution from noisy data, *Journal of Fourier Analysis and Applications* **19**, 1229 (2013).
- [38] C. Fernandez-Granda, Super-resolution of point sources via convex programming, *Information and Inference: A Journal of the IMA* **5**, 251 (2016).
- [39] V. Duval and G. Peyré, Exact support recovery for sparse spikes deconvolution, *Foundations of Computational Mathematics* **15**, 1315 (2015).
- [40] T. B. Van Driel, S. Nelson, R. Armenta, G. Blaj, S. Boo, S. Boutet, D. Doering, A. Dragone, P. Hart, G. Haller, *et al.*, The epix10k 2-megapixel hard x-ray detector at lcls, *Journal of synchrotron radiation* **27** (2020).
- [41] D. Slepian, Prolate spheroidal wave functions, fourier analysis, and uncertainty—v: The discrete case, *Bell System Technical Journal* **57**, 1371 (1978).
- [42] Y. Liu, S. L. Horton, J. Yang, J. P. F. Nunes, X. Shen, T. J. A. Wolf, R. Forbes, C. Cheng, B. Moore, M. Centurion, K. Hegazy, R. Li, M.-F. Lin, A. Stolow, P. Hockett, T. Rozgonyi, P. Marquetand, X. Wang, and T. Weinacht, Spectroscopic and structural probing of excited-state molecular dynamics with time-resolved photoelectron spectroscopy and ultrafast electron diffraction, *Phys. Rev. X* **10**, 021016 (2020).
- [43] M. Grant and S. Boyd, Cvx: Matlab software for disciplined convex programming, version 2.1 (2014).
- [44] H. Zou and T. Hastie, Regularization and variable selection via the elastic net, *Journal of the royal statistical society: series B (statistical methodology)* **67**, 301 (2005).
- [45] P. Catala, V. Duval, and G. Peyré, A low-rank approach to off-the-grid sparse superresolution, *SIAM Journal on Imaging Sciences* **12**, 1464 (2019).